

# Computational design of tunnel diodes with negative differential resistance and ultrahigh peak-to-valley current ratio based on two-dimensional cold metals: The case of $\text{NbSi}_2\text{N}_4/\text{HfSi}_2\text{N}_4/\text{NbSi}_2\text{N}_4$ lateral heterojunction diode

P. Bodewei<sup>\*</sup>, E. Şaşioğlu<sup>DOI</sup>, N.F. Hinsche<sup>DOI</sup>, and I. Mertig

*Institute of Physics, Martin Luther University Halle-Wittenberg, 06120 Halle (Saale), Germany*



(Received 10 January 2024; revised 11 April 2024; accepted 7 June 2024; published 1 July 2024)

Cold metals have recently gained attention as a promising platform for innovative devices, such as tunnel diodes with negative differential resistance (NDR) and field-effect transistors with subthreshold swings below the thermionic limit. Recently discovered two-dimensional (2D)  $MA_2Z_4$  ( $M = \text{Ti}, \text{Zr}, \text{Hf}, \text{Nb}, \text{Ta}; A = \text{Si}, \text{Ge}; Z = \text{N}, \text{P}$ ) compounds exhibit both cold-metallic and semiconducting behavior. In this work, we present a computational study of lateral heterojunction tunnel diodes based on 2D  $\text{NbSi}_2\text{N}_4$  and  $\text{HfSi}_2\text{N}_4$  compounds. Employing density-functional theory combined with a nonequilibrium Green-function method, we investigate the current-voltage ( $I-V$ ) characteristics of lateral tunnel diodes with varying barrier thicknesses in both zigzag and armchair orientations. We find that tunnel diodes in the zigzag orientation exhibit significantly higher peak current densities, while those in the armchair orientation display larger peak-to-valley current ratios (PVCRs) compared to the zigzag orientation. Our findings suggest that  $MA_2Z_4$  materials are promising candidates for realizing NDR tunnel diodes with ultrahigh PVCR values, which could have potential applications in memory, logic circuits, and other electronic devices.

DOI: 10.1103/PhysRevApplied.22.014004

## I. INTRODUCTION

Negative-differential-resistance (NDR) tunnel diodes offer unique functionalities and potential applications when integrated within conventional complementary metal oxide semiconductor (CMOS) transistors [1]. These include NDR-based multivalued logic gates, static random-access memory (SRAM), magnetic random-access memory, and low-power oscillators [2–4]. Exploiting the NDR effect allows for logic and memory architectures with reduced device count, higher speed, and lower power consumption. For example, a tunnel SRAM requires only one transistor and two NDR tunnel diodes, instead of the six transistors in a conventional SRAM. This results in a smaller footprint and lower power consumption [4,5]. NDR diodes can be combined with CMOS transistors to implement various logic gates, while the extension to multivalued logic increases information density and decreases system complexity [6–8].

The NDR effect has been demonstrated in a variety of devices and circuits, with a focus on two-terminal tunnel diodes, like Esaki diodes and resonant tunneling diodes [9–12]. Esaki diodes, which operate via quantum tunneling under forward bias, show NDR behavior. However, the application of these two-terminal NDR diodes

faces challenges. They often have low peak-to-valley current ratios (PVCRs), which are not suitable for memory applications like tunnel SRAMs [11,13–15]. Additionally, III-V semiconductors, which offer high PVCR, are difficult to integrate within current CMOS technology [16,17]. Research efforts have sought to enhance PVCR values over 100 through CMOS-compatible processes [4]. While some NDR circuits show extremely high PVCR values, their complex topology with multiple transistors makes them unsuitable for memory applications [18–22].

Existing semiconductor-based NDR tunnel diodes suffer from low PVCR values, which is attributed to the band tail tunneling that originates from the strong doping and dopant fluctuations [23–25]. To address this issue, we recently proposed a new semiconductor-free NDR tunnel diode concept with ultrahigh PVCR [26]. Our proposed diode consists of two cold-metal electrodes separated by a thin insulating tunnel barrier (see Fig. 1). The NDR effect arises from the unique electronic band structure of the cold-metal electrodes (see Fig. 2). A cold metal is obtained when the metallic, i.e., partially filled, bands are separated from all energetically higher- and lower-lying bands by sufficiently large energy gaps. Specifically, the width of the isolated metallic bands around the Fermi level, as well as the energy gaps separating higher- and lower-lying bands, determine the current-voltage ( $I-V$ ) characteristics and PVCR of the tunnel diode. By choosing the

\*Contact author: paul.bodewei@student.uni-halle.de

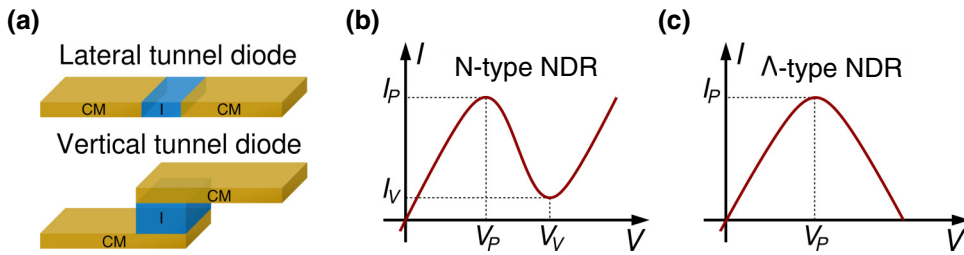


FIG. 1. (a) Schematic representation of lateral and vertical negative-differential-resistance tunnel diodes based on cold metals. CM and I stand for cold metal and insulator, respectively. (b),(c) The  $I$ - $V$  characteristics showing (b) conventional N-type and (c)  $\Lambda$ -type NDR.

appropriate cold-metal electrode materials, either a conventional N-type or  $\Lambda$ -type NDR effect can be achieved as sketched in Figs. 1(b) and 1(c).

The intention of this paper is to computationally design lateral heterojunction NDR tunnel diodes based on the recently discovered family of two-dimensional (2D) materials known as  $MA_2Z_4$  (where  $M = \text{Ti}, \text{Zr}, \text{Hf}, \text{Nb}, \text{Ta}$ ;  $A = \text{Si}, \text{Ge}$ ;  $Z = \text{N}, \text{P}$ ) [27]. These  $MA_2Z_4$  compounds provide an exceptional platform for realizing NDR tunnel diodes due to their closely matched lattice parameters and composition, as well as their ability to exhibit both cold-metallic and semiconducting properties within the same material class [28]. This characteristic enables the coherent growth of consecutive components within the device, which naturally favors a lateral device geometry [29]. Furthermore, we prefer a lateral heterojunction design rather than the vertical counterpart, as a higher current density can be expected, especially pronounced in van der Waals 2D materials [30]. An additional benefit of the  $MA_2Z_4$  compounds is their superior strength and mechanical stability compared to most monolayer semiconductors like  $\text{MoS}_2$  [28]. Additionally, the electronic

properties of  $MA_2Z_4$  compounds are more resilient when it comes to stacking. For example, the cold-metallic behavior observed in  $MX_2$  (where  $M = \text{Nb}, \text{Ta}$ ;  $X = \text{S}, \text{Se}, \text{Te}$ ) is typically limited to monolayers, disappearing after only a few layers [31]. In contrast,  $MA_2Z_4$  compounds maintain this behavior even in their bulk phase.

## II. COMPUTATIONAL METHOD

The computational design of the presented lateral heterojunction tunnel diodes is based on density-functional theory (DFT) within the QuantumATK T-2022.03 package [32]. We used a linear combination of atomic orbitals (LCAO) basis set (double-zeta-polarized) with norm-conserving FHI (Fritz-Haber Institute) pseudopotentials [33]. The exchange-correlation functional was represented by a generalized gradient approximation (GGA) with Perdew-Burke-Ernzerhof (PBE) flavor [34]. The self-consistent DFT calculations are performed using a  $24 \times 24 \times 1$   $k$ -point grid with a density mesh cut-off of 45 Hartree and the total energy converged to at least  $10^{-4}$  Hartree. To prevent interactions between the periodically repeated images, 20 Å of vacuum were added, and Dirichlet and Neumann boundary conditions are employed. The transport calculations were performed using DFT combined with a nonequilibrium Green-function method (NEGF). We use a  $24 \times 1 \times 184$  (respectively  $14 \times 1 \times 318$ )  $k$ -point grid in self-consistent DFT-NEGF calculations of the lateral tunnel diodes along the armchair (respectively zigzag) orientation.

The  $I$ - $V$  characteristics were calculated within a Landauer approach [35], where  $I(V) = (2e/h) \int T(E, V) [f_L(E, V) - f_R(E, V)] dE$ . Here  $V$  denotes the bias voltage,  $T(E, V)$  are the transmission coefficients, and  $f_L(E, V)$  and  $f_R(E, V)$  are the Fermi-Dirac distributions of the left and right electrodes, respectively. The temperature was kept at  $T = 300$  K throughout all calculations. The transmission coefficients  $T(E, V)$  for the lateral tunnel diodes along the armchair (respectively zigzag) orientation are calculated using a  $255 \times 1$  (respectively  $147 \times 1$ )  $k$ -point grid; convergence tests can be found in the Supplemental Material [36].

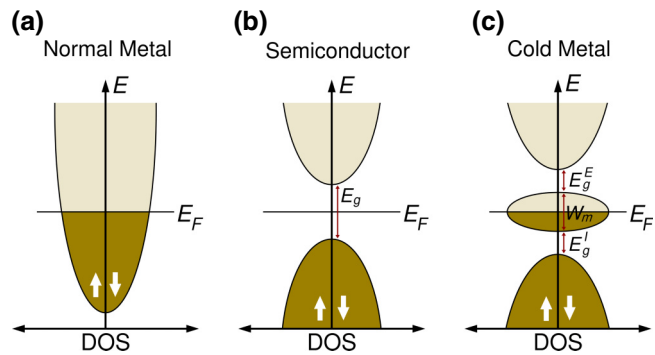


FIG. 2. Schematic illustration of the density of states (DOS) depicting (a) a normal metal, (b) a semiconductor, and (c) a cold metal. The symbols  $E_g$ ,  $E_g^I$ , and  $E_g^E$  correspond to the band gap of the semiconductor, as well as the internal and external band gaps of the cold metal, respectively. The width of the metallic band for the cold metal is designated by  $W_m$ . The Fermi level is denoted by  $E_F$ .

### III. RESULTS AND DISCUSSION

In Fig. 1 we present schematically the structures of the lateral and vertical NDR tunnel diodes and the corresponding  $I$ - $V$  characteristics. The concept of the cold-metal NDR tunnel diode was previously introduced by us in Ref. [26], and thus only a brief overview of the device will be given subsequently. Our NDR tunnel diode consists of two cold-metal electrodes, which are separated by an insulating tunnel barrier. The schematic density of states (DOS) of a cold metal is presented in Fig. 2 and compared with the DOS of a conventional metal and a semiconductor. As seen in the schematic DOS cold-metallic materials possess a unique band structure that has an isolated metallic band  $W_m$  around the Fermi level as well as energy gaps separating higher- and lower-lying states. The latter is referred to as the internal gap  $E_g^I$  (below the Fermi level) and external  $E_g^E$  (above the Fermi level). These three electronic structure parameters play a decisive role in determining the  $I$ - $V$  characteristics of the tunnel diode and the type of the NDR effect [see Fig. 1(b)]. A conventional N-type NDR effect is expected if these three parameters  $W_m$ ,  $E_g^I$ , and  $E_g^E$  are close to each other. On the other hand, the tunnel diode will show a  $\Lambda$ -type NDR effect if  $W_m \ll E_g^I \sim E_g^E$ .

To design lateral NDR tunnel diodes, we first performed a material screening within the  $\text{MoSi}_2\text{N}_4$  compound family, specifically focusing on the cold-metallic and semiconducting compounds, which are listed in Table I. Our selection criteria for materials included cold-metal electrode materials with large internal ( $E_g^I$ ) and external ( $E_g^E$ ) band gaps relative to their metallic band widths ( $W_m$ ). For tunnel barriers, we chose materials with large band gaps ( $E_g$ ) and work functions that matched those of the cold-metallic compounds. In Table I, we provide the lattice parameters, work functions, band gaps ( $E_g^I$ ,  $E_g^E$ ,  $E_g$ ), and band widths for all the selected compounds. As presented,

TABLE I. Lattice constant  $a_0$ , work function  $\Phi$ , band gap  $E_g$ , internal gap  $E_g^I$ , external gap  $E_g^E$ , and metallic bandwidth  $W_m$  of cold-metallic and semiconducting  $MA_2Z_4$  ( $M = \text{Nb}, \text{Ta}, \text{Ti}, \text{Zr}, \text{Hf}; A = \text{Si}, \text{Ge}; Z = \text{N}, \text{P}$ ) monolayers. Lattice parameters are taken from Ref. [28]. The band gap of  $\text{HfSi}_2\text{N}_4$  calculated within the GGA +  $U$  method is given in parentheses.

Compound	$a_0$ (Å)	$\Phi$ (eV)	$E_g$ (eV)	$E_g^I$ (eV)	$E_g^E$ (eV)	$W_m$ (eV)
$\text{NbSi}_2\text{N}_4$	2.97	5.62		1.01	1.74	1.33
$\text{NbGe}_2\text{N}_4$	3.08	5.69		0.92	1.21	1.16
$\text{NbSi}_2\text{P}_4$	3.53	4.52		0.01	0.52	1.26
$\text{TaSi}_2\text{N}_4$	2.97	5.47		1.16	1.41	1.56
$\text{TaGe}_2\text{N}_4$	3.08	5.51		1.16	0.98	1.25
$\text{TaSi}_2\text{P}_4$	3.53	4.45		0.00	0.27	1.51
$\text{TiSi}_2\text{N}_4$	2.94	6.08	1.54			
$\text{ZrSi}_2\text{N}_4$	3.04	5.94	1.46			
$\text{HfSi}_2\text{N}_4$	3.03	5.92	1.61 (1.84)			

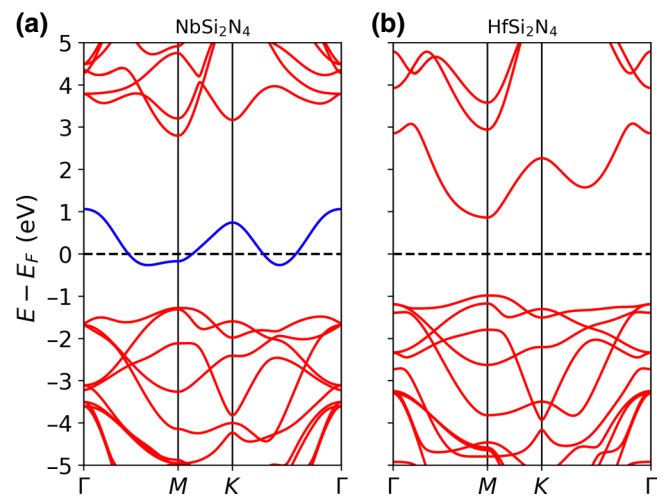


FIG. 3. Calculated PBE band structure of monolayer  $\text{NbSi}_2\text{N}_4$  and PBE +  $U$  band structure of  $\text{HfSi}_2\text{N}_4$  along the high-symmetry lines in the 2D Brillouin zone. The dashed black lines denote the Fermi level, which is set to zero. The isolated metallic band of the  $\text{NbSi}_2\text{N}_4$  is highlighted in blue.

all the cold-metal compounds under consideration, with few exceptions, have either internal or external band gaps smaller than their corresponding band widths, indicating that tunnel diodes based on these materials would exhibit the conventional N-type NDR effect.

Among the screened materials, we selected  $\text{NbSi}_2\text{N}_4$  as the cold-metal electrode and  $\text{HfSi}_2\text{N}_4$  as the tunnel barrier for our lateral tunnel diode simulations. The calculated electronic band structures of these materials are presented in Fig. 3. As all members of the 2D  $\text{MoSi}_2\text{N}_4$  compound family belong to the trigonal  $P\bar{6}m2$  (#187) space group, the bands are shown along the high-symmetry points of the related hexagonal Brillouin zone. The monolayer  $\text{NbSi}_2\text{N}_4$  possesses internal and external band gaps of 1.01 and 1.74 eV within DFT-PBE. The tunnel barrier  $\text{HfSi}_2\text{N}_4$  has a band gap of 1.61 eV within DFT-PBE. Note that DFT-PBE underestimates the band gap of semiconductors and insulators, as well as cold metals, including cold metals such as  $MX_2$  ( $M = \text{Nb}, \text{Ta}; X = \text{S}, \text{Se}, \text{Te}$ ) compounds [37,38]. To improve the band gap of the tunnel barrier  $\text{HfSi}_2\text{N}_4$ , we employed a PBE +  $U$  method with a  $U$  value of 8 eV for the  $d$  orbitals of Hf in the transport calculations (see Table I).

In Fig. 4, we show the atomic structure of the lateral tunnel diode, which is formed by attaching one monolayer of cold metal  $\text{NbSi}_2\text{N}_4$  as the left and right electrodes and one monolayer of  $\text{HfSi}_2\text{N}_4$  as the tunnel barrier. We consider both armchair and zigzag directions as the transport direction for the tunnel diodes, which we will refer to as armchair and zigzag tunnel diodes, respectively. The device is periodic in the  $x$  direction, and we choose the  $z$  direction as the transport direction. Since the lattice

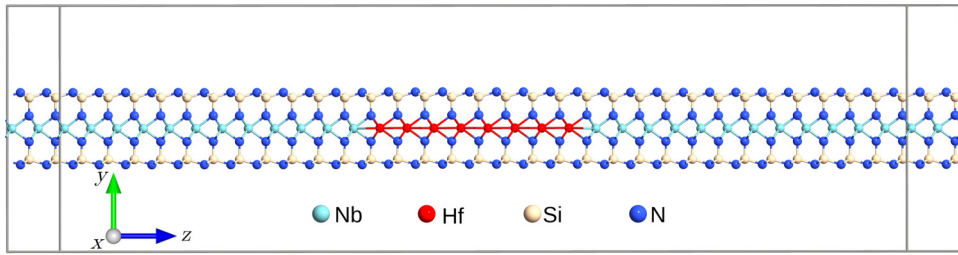


FIG. 4. Schematic illustration of the atomic structure of the  $\text{NbSi}_2\text{N}_4/\text{HfSi}_2\text{N}_4/\text{NbSi}_2\text{N}_4$  lateral heterojunction tunnel diode device in armchair orientation. The tunnel barrier width is 21 Å. Different atomic components are represented by distinct colors.

constants of the electrode and tunnel barrier materials are slightly different (less than 2% mismatch, see Table I) for both directions, the tunnel barrier adopts the in-plane ( $x$  direction) lattice constant of the electrode material, and its lattice constant along the transport direction ( $z$  direction) is relaxed. The tunnel barrier thicknesses are chosen to be about 21 and 30 Å for both armchair and zigzag tunnel diodes. The total length of the scattering region ranges from 81 to 90 Å.

In Fig. 5, we present the calculated  $I$ - $V$  curves for tunnel diodes with tunnel barrier widths of 21 and 30 Å, for both armchair (black lines) and zigzag (red lines) directions. A maximum bias voltage of 1.5 V was chosen. We report a conventional N-type NDR effect in both transport directions with a valley voltage  $V_V$  of approximately 1.25 V, which is primarily set by the metallic band width of the cold-metal electrodes (see Table I). Besides this similarity, the  $I$ - $V$  curves of the armchair and zigzag directions exhibit distinct behavior. In the armchair case, the peak current  $I_P$  (cf. Fig. 2) is achieved at very low bias voltages of about 0.2 V, while in the zigzag case it appears at higher bias voltages of  $V > 0.7$  V. These details can be directly attributed to the overlap of contributing electronic states of the left and right cold metal electrodes in different

areas of the Brillouin zone. The mentioned overlaps differ for armchair- and zigzag-oriented tunnel diodes, resulting in the  $I$ - $V$  curves presented in Fig. 5.

In a first approximation, the spin-independent transmission through an insulating barrier of width  $d$  at zero bias is  $T(k_z, E) = t_L(k_z, E) \exp[-2\kappa(k_z, E)d]t_R(k_z, E)$  [39]. Here  $t_L(k_z, E)$  and  $t_R(k_z, E)$  are the interface transmission functions of the left and right metallic leads, respectively. Assuming perfect symmetry matching of the wave functions at the interfaces, the product  $t_L(k_z, E)t_R(k_z, E)$  coincides with the joint density of states of left and right electrodes. The remaining factor involves the exponential decay length  $1/\kappa(k_z, E)$  of the wave function within the insulating barrier. The latter is directly connected to the complex band structure  $E(k_z + ik)$  of the barrier, which will be discussed later in this paper. We introduce further insights on the specific structure of the  $I$ - $V$  curves maxima via the energy- and state-resolved transmission, as well as projected interface band structures in the Supplemental Material [36].

From Fig. 5 we furthermore identify vanishing valley current in a rather large bias voltage interval of 1.0 to 1.3 V for armchair tunnel diodes at both barrier thicknesses. We note that this is in contrast to conventional Esaki diodes,

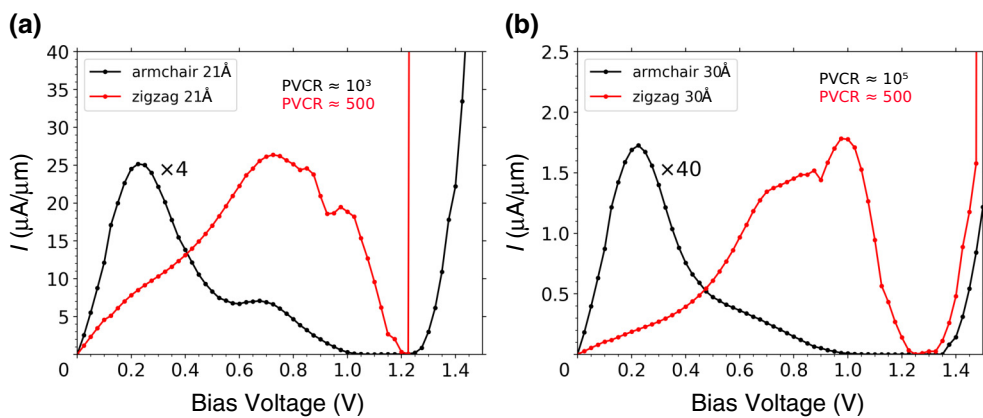


FIG. 5. (a) Calculated room-temperature current-voltage characteristics for the  $\text{NbSi}_2\text{N}_4/\text{HfSi}_2\text{N}_4/\text{NbSi}_2\text{N}_4$  lateral heterojunction tunnel diode with 21-Å tunnel barrier in both armchair and zigzag orientations. (b) The same as panel (a) for a tunnel barrier length of 30 Å.

where a vanishing valley current is barely obtainable. For the zigzag tunnel diodes, the transition from the NDR to second positive differential resistance (PDR) takes place in a very narrow voltage window. Note that for the first PDR and NDR regions the current is formed by intraband tunneling, i.e., from the single Nb  $d$  band in the  $\text{NbSi}_2\text{N}_4$  electrodes, while in the second PDR region, the current is due to interband tunneling.

The most striking difference is the absolute value of the peak current density in both device geometries. The maximum current density of the armchair tunnel diode located close to 0.25 V is noticeably smaller than the peak current density of the zigzag tunnel diode located at  $V > 0.7$  V. In particular, we find a current density ratio of  $I_{zz}/I_{\text{arm}} \approx 4$  for the shorter 21-Å device and  $I_{zz}/I_{\text{arm}} \approx 40$  for the longer 30-Å device. This difference can be readily explained with the help of the complex band structure  $E(k_z + ik)$ , whereas  $\kappa = \text{Im } k_z$ . The latter is displayed for the tunnel barrier material  $\text{HfSi}_2\text{N}_4$  for both device orientations in Fig. 6.

We recall that the transmission  $T(k_z, E) = t_L(k_z, E) \exp[-2\kappa(k_z, E)d]t_R(k_z, E)$  through an insulating barrier is, to a good approximation, dependent only on the available state overlap of the left and right electrodes, their interface symmetry matching, and the exponential decay length  $1/\kappa(k_z, E)$  within the insulating barrier. It is worth mentioning that, in the case of the orthorhombic transport geometry of the explicit diode devices, the available states of the electrodes as well as barrier material within the range of the applied bias voltages consist only of  $A'$  and  $A''$  symmetry characters of the  $C_{1h}$  group, i.e., states symmetric or antisymmetric with respect to reflection through the Hf/Nb mirror plane [40,41]. As a consequence, there is almost no state filtering at the interface and the electronic transport

can be well understood by an analysis of the complex band structure. Obviously states with a small imaginary part  $\kappa$  will have the weakest decay within the  $\text{HfSi}_2\text{N}_4$  barrier and will dominate the contribution to the transmission, i.e., the current density.

From Fig. 6 it is seen that the fundamental band gap for real-valued  $k_z$  is bridged by loops with imaginary-valued  $\kappa = \text{Im } k_z$ . Comparing the complex band structures of the zigzag- and armchair-oriented barrier materials, we immediately conclude that a single loop will dictate the transport in the zigzag geometry, while a combination of at least two crossing loops will describe the tunneling in the case of the armchair geometry. In all cases, imaginary loops have to connect real-valued  $k_z$  of the same symmetry character [42]. The fact that an imaginary loop in the zigzag direction is considerably smaller than one in the armchair direction directly reflects the reduced size of the current densities shown in Fig. 5. For simplicity we let  $E = E_F$  and we find minimal values of  $\kappa_{zz} \approx 0.22 \text{ 1/}\text{\AA}$  and  $\kappa_{\text{arm}} \approx 0.32 \text{ 1/}\text{\AA}$  for the mid-gap states. Approximating the current density by  $I \approx \exp[-\kappa(k_z = 0, E_F)d]$ , we will obtain ratios of  $I_{zz}/I_{\text{arm}} \approx 8$  for the shorter 21-Å device and  $I_{zz}/I_{\text{arm}} \approx 20$  for the longer 30-Å device, which is in excellent qualitative agreement with the results of our full NEGF calculations presented in Fig. 5. Because of the evanescent nature of the states, the ratio  $I_{zz}/I_{\text{arm}}$  will naturally increase for larger barrier widths.

While the peak current density in zigzag tunnel diodes is notably higher, it is essential to note that these exhibit smaller PVCR values. The PVCR values obtained for both tunnel barrier thicknesses are approximately 500. In contrast, for armchair tunnel diodes, the PVCR values are significantly higher, reaching  $10^3$  and  $10^5$  for tunnel

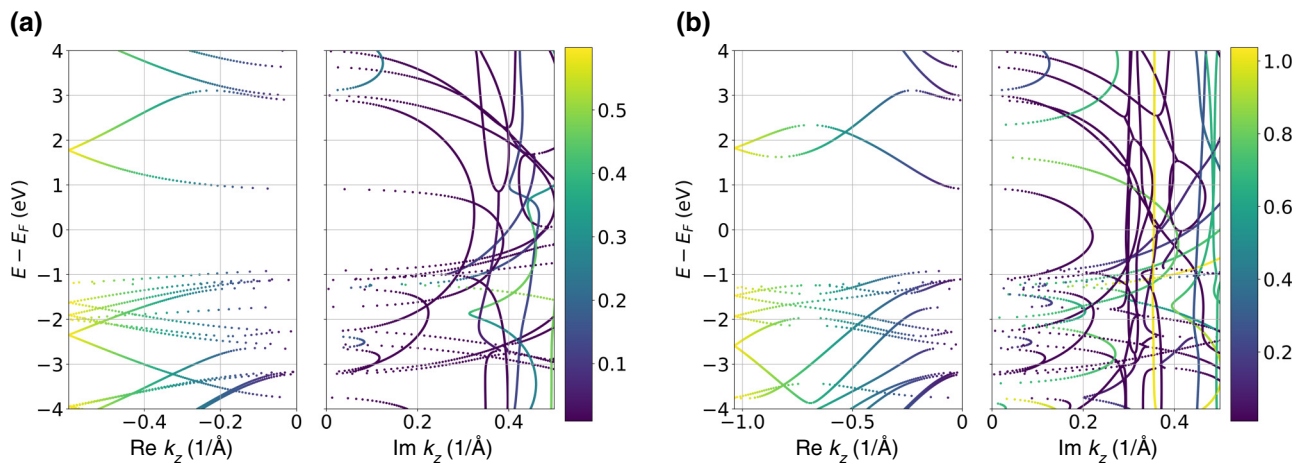


FIG. 6. The left-hand panels show the complex band structures of the barrier material  $\text{HfSi}_2\text{N}_4$  in the (a) armchair and (b) zigzag directions. The corresponding right-hand panels show the imaginary parts  $\kappa = \text{Im } k_z$  of the, in general complex, wave vector  $k_z$ . The color bar reflects the value of the real part of  $k_z$ , i.e., purple bands indicate imaginary bands of the first kind with  $\text{Re } k_z = 0$ ; yellow bands correspond to imaginary bands of the second kind with  $\text{Re } k_z = \text{max}$ , and all other colors refer to complex bands with  $\text{Re } k_z \neq 0$  and  $\text{Im } k_z \neq 0$ .

barriers of 21 and 30 Å, respectively. These findings highlight the trade-off between peak current density and PVCR, and the unique characteristics of armchair and zigzag tunnel diodes for diverse applications. We note that these PVCR values are orders of magnitudes higher than found in conventional Ge-based NDR diodes ( $\text{PVCR} \approx 2\text{--}10$ ), in  $\text{CaF}_2$ -based NDR diodes ( $\text{PVCR} \approx 100$ ) [1], or even in  $\text{MoS}_2$  homojunctions with a  $\text{PVCR} \approx 200\text{--}400$  [30].

We want to emphasize that the choice of pseudopotentials and basis sets can be crucial in the evaluation of the complex band structure and thus of the related  $I\text{-}V$  characteristics within the LCAO-NEGF formalism. One should pay attention to the vertical complex bands appearing with an almost constant decay length  $1/\kappa_z$  over a wide energy range, e.g., the imaginary band of second kind at  $\kappa = \text{Im } k_z \approx 0.35 \text{ 1/Å}$  in the case of zigzag orientation shown in Fig. 6(b). These spurious states, referred to as *ghost* or *phantom* modes, are associated with virtual molecular orbitals of the barrier area and might lead to an inaccurate description of the tunneling [43]. Interestingly, the ghost modes are an apparently unavoidable consequence of large numerical basis sets, so an alleged increase in computational accuracy might increase the number of ghost states [43]. A separation of ghost modes and *true* complex band structure modes is challenging. In our case, the ghost states do have large  $\kappa$ , are heavily damped, and thus contribute only negligibly to the transport. Generally, they may exhibit very slow decay and can dominate the transport, leading to fundamental qualitative and quantitative errors. We suggest using the complex band structure and its validity concerning the ghost states as a first test before the computationally demanding Landauer approach is applied.

The  $I\text{-}V$  characteristics and high PVCR values reported for the tunnel diodes are based on the assumption of coherent tunneling transport. This means that mechanisms like electron-electron scattering or electron-phonon scattering are not included in the calculations. Electron-phonon scattering is a well-known dissipation mechanism, particularly efficient in 2D semiconductors compared to three-dimensional ones [44]. It can influence current flow in devices based on 2D materials [45]. While software packages like QuantumATK can include electron-phonon scattering, the computational cost is significant and often limited to very simple models [46]. Therefore, for our presented tunnel diodes, such detailed simulations are currently not practical. Consequently, the peak current in Fig. 5 and the PVCR obtained here represent upper limits within the coherent tunneling framework. Introducing inelastic scattering mechanisms, like electron-phonon interactions, is expected to modify the  $I\text{-}V$  characteristics. This would likely decrease the peak current and increase the valley current, resulting in a lower PVCR value. It is important to note that other factors, such as defects, interface atomic mixing, and interactions with surrounding materials, can also influence the  $I\text{-}V$

characteristics. However, the overall trends observed in the  $I\text{-}V$  curves are expected to remain largely unchanged.

Finally, we discuss the anticipated  $I\text{-}V$  characteristics of tunnel diodes based on other cold metals listed in Table I. As mentioned, the N-type NDR effect is expected to be common in tunnel diodes using these materials. For example,  $\text{TaSi}_2\text{N}_4$ , which is isoelectronic to  $\text{NbSi}_2\text{N}_4$ , is expected to exhibit qualitatively similar  $I\text{-}V$  curves. However, quantitative differences, such as peak current density, valley voltage, and valley current, are likely due to the larger metallic band width ( $W_m$ ) and slightly smaller internal and external band gaps of  $\text{TaSi}_2\text{N}_4$ . Similarly, Ge-based compounds are expected to exhibit analogous  $I\text{-}V$  characteristics. On the other hand, tunnel diodes based on P-containing compounds like  $\text{NbSi}_2\text{P}_4$  may exhibit significantly smaller PVCR values, primarily due to the vanishing internal band gap in these compounds. This insight into the expected behavior of tunnel diodes based on various cold metals offers a glimpse into the diverse possibilities for tailoring their performance in electronic applications and underscores the role of material properties in shaping device behavior.

#### IV. CONCLUSIONS

In conclusion, our computational investigation of prototype lateral heterojunction tunnel diodes unveils the remarkable potential of cold-metallic  $MA_2Z_4$  ( $M = \text{Nb}, \text{Ta}; A = \text{Si}, \text{Ge}; Z = \text{N}, \text{P}$ ) compounds for harnessing the NDR phenomenon with very high PVCR values orders of magnitude higher than in conventional NDR tunnel diodes. By considering the exemplary cold metal  $\text{NbSi}_2\text{N}_4$  as the prototype electrode material and  $\text{HfSi}_2\text{N}_4$  as the tunnel barrier, our calculations consistently demonstrate the achievement of N-type NDR behavior in both armchair- and zigzag-oriented tunnel diodes. Moreover, our findings reveal intriguing differences between these orientations. Zigzag-oriented tunnel diodes exhibit significantly higher peak current densities, indicating their potential for high-speed electronic applications, while armchair-oriented diodes achieve very high PVCR values. This duality in performance highlights the versatility of  $MA_2Z_4$  materials and their promising role in enabling future electronic devices with enhanced functionality and efficiency. Our findings not only broaden our understanding of the NDR effect in cold-metal-based heterojunction tunnel diodes, but also pave the way for exciting new directions in materials engineering for next-generation electronics.

#### ACKNOWLEDGMENTS

This work was supported by SFB CRC/TRR 227 of the Deutsche Forschungsgemeinschaft (DFG) and by the European Union (EFRE) via Grant No. ZS/2016/06/79307.

- [1] P. R. Berger and A. Ramesh, in *Comprehensive Semiconductor Science and Technology* (Elsevier Inc., United States, 2011), p. 176.
- [2] S. B. Jo, J. Kang, and J. H. Cho, Recent advances on multivalued logic gates: A materials perspective, *Adv. Sci.* **8**, 2004216 (2021).
- [3] S. Wang, A. Pan, C. Grezes, P. K. Amiri, K. L. Wang, C. O. Chui, and P. Gupta, Leveraging nMOS negative differential resistance for low power, high reliability magnetic memory, *IEEE Trans. Electron Devices* **64**, 4084 (2017).
- [4] J. P. A. van der Wagt, Tunneling-based SRAM, *Proc. IEEE* **87**, 571 (1999).
- [5] K. Karda, J. Brockman, S. Sutar, A. Seabaugh, and J. Nahas, in *2009 IEEE International Conference on IC Design and Technology* (IEEE, Austin, TX, USA, 2009), p. 233.
- [6] L. J. Micheel and M. J. Paulus, in *Proceedings of the Twentieth International Symposium on Multiple-Valued Logic* (IEEE Computer Society, Los Alamitos, CA, USA, 1990), p. 189.
- [7] H. Lin, in *Proceedings of 24th International Symposium on Multiple-Valued Logic (ISMVL'94)* (IEEE, Boston, MA, USA, 1994), p. 188.
- [8] N. Jin, S.-Y. Chung, R. M. Heyns, P. R. Berger, R. Yu, P. E. Thompson, and S. L. Rommel, Tri-state logic using vertically integrated Si-SiGe resonant interband tunneling diodes with double NDR, *IEEE Electron Device Lett.* **25**, 646 (2004).
- [9] L. Esaki, New phenomenon in narrow germanium *p-n* junctions, *Phys. Rev.* **109**, 603 (1958).
- [10] L. Esaki and R. Tsu, Superlattice and negative differential conductivity in semiconductors, *IBM J. Res. Dev.* **14**, 61 (1970).
- [11] A. Ramesh, P. R. Berger, and R. Loo, High 5.2 peak-to-valley current ratio in Si/SiGe resonant interband tunnel diodes grown by chemical vapor deposition, *Appl. Phys. Lett.* **100**, 092104 (2012).
- [12] A. V. Bruce, S. Liu, J. N. Fry, and H.-P. Cheng, Insights into negative differential resistance in MoS<sub>2</sub> Esaki diodes: A first-principles perspective, *Phys. Rev. B* **102**, 115415 (2020).
- [13] W. Y. Fung, L. Chen, and W. Lu, Esaki tunnel diodes based on vertical Si-Ge nanowire heterojunctions, *Appl. Phys. Lett.* **99**, 092108 (2011).
- [14] R. Duschl, O. Schmidt, G. Reitemann, E. Kasper, and K. Eberl, High room temperature peak-to-valley current ratio in Si based Esaki diodes, *Electron. Lett.* **35**, 1111 (1999).
- [15] H. Schmid, C. Bessire, M. T. Björk, A. Schenk, and H. Riel, Silicon nanowire Esaki diodes, *Nano Lett.* **12**, 699 (2012).
- [16] D. Chow, J. Schulman, E. Özbay, and D. Bloom, Investigation of In<sub>0.53</sub>Ga<sub>0.47</sub>As/AlAs resonant tunneling diodes for high speed switching, *Appl. Phys. Lett.* **61**, 1685 (1992).
- [17] H. Tsai, Y. Su, H. Lin, R. Wang, and T. Lee, PN double quantum well resonant interband tunneling diode with peak-to-valley current ratio of 144 at room temperature, *IEEE Electron Device Lett.* **15**, 357 (1994).
- [18] S.-Y. Chung, N. Jin, P. R. Berger, R. Yu, P. E. Thompson, R. Lake, S. L. Rommel, and S. K. Kurinec, Three-terminal Si-based negative differential resistance circuit element with adjustable peak-to-valley current ratios using a monolithic vertical integration, *Appl. Phys. Lett.* **84**, 2688 (2004).
- [19] S.-L. Chen, P. B. Griffin, and J. D. Plummer, Negative differential resistance circuit design and memory applications, *IEEE Trans. Electron Devices* **56**, 634 (2009).
- [20] K.-J. Gan, C.-S. Tsai, and W.-L. Sun, Fabrication and application of MOS-HBT-NDR circuit using standard SiGe process, *Electron. Lett.* **43**, 1 (2007).
- [21] R. Duane, A. Mathewson, and A. Concannon, Bistable gated bipolar device, *IEEE Electron Device Lett.* **24**, 661 (2003).
- [22] L. Fang, C. Qiu, H. Zhang, Y. Hu, and L.-M. Peng, Giant negative differential resistance effect caused by cutting off acceptable quantum states in carbon nanotube tunneling devices, *Adv. Electron. Mater.* **8**, 2101314 (2022).
- [23] S. Sant and A. Schenk, The effect of density-of-state tails on band-to-band tunneling: Theory and application to tunnel field effect transistors, *J. Appl. Phys.* **122**, 135702 (2017).
- [24] J. Bizindavyi, A. S. Verhulst, Q. Smets, D. Verreck, B. Sorée, and G. Groeseneken, Band-tails tunneling resolving the theory-experiment discrepancy in Esaki diodes, *IEEE J. Electron Devices Soc.* **6**, 633 (2018).
- [25] A. Schenk and S. Sant, Tunneling between density-of-state tails: Theory and effect on Esaki diodes, *J. Appl. Phys.* **128**, 014502 (2020).
- [26] E. Şaşioğlu and I. Mertig, Theoretical prediction of semiconductor-free negative differential resistance tunnel diodes with high peak-to-valley current ratios based on two-dimensional cold metals, *ACS Appl. Nano Mater.* **6**, 3758 (2023).
- [27] Y.-L. Hong, Z. Liu, L. Wang, T. Zhou, W. Ma, C. Xu, S. Feng, L. Chen, M.-L. Chen, D.-M. Sun *et al.*, Chemical vapor deposition of layered two-dimensional MoSi<sub>2</sub>N<sub>4</sub> materials, *Science* **369**, 670 (2020).
- [28] Y. Yin, Q. Gong, M. Yi, and W. Guo, Emerging versatile two-dimensional MoSi<sub>2</sub>N<sub>4</sub> family, *Adv. Funct. Mater.* **33**, 2214050 (2023).
- [29] N. Ichinose, M. Maruyama, Z. L. Takato Hotta, R. Canton-Vitoriaa, S. Okada, F. Zeng, T. T. Feng Zhang, K. Watanabe, and R. Kitaura, Two-dimensional atomic-scale ultrathin lateral heterostructures, *arXiv:2208.12696v2*.
- [30] A. V. Bruce, S. Liu, J. N. Fry, and H.-P. Cheng, Insights into negative differential resistance in MoS<sub>2</sub> Esaki diodes: A first-principles perspective, *Phys. Rev. B* **102**, 115415 (2020).
- [31] N. F. Hinsche and K. S. Thygesen, Electron–phonon interaction and transport properties of metallic bulk and monolayer transition metal dichalcogenide TaS<sub>2</sub>, *2D Mater.* **5**, 015009 (2017).
- [32] S. Smidstrup, T. Markussen, P. Vancraeyveld, J. Wellendorff, J. Schneider, T. Gunst, B. Verstichel, D. Stradi, P. A. Khomyakov, U. G. Vej-Hansen *et al.*, QuantumATK: An integrated platform of electronic and atomic-scale modelling tools, *J. Phys: Condens. Matter* **32**, 015901 (2020).
- [33] N. Troullier and J. L. Martins, Efficient pseudopotentials for plane-wave calculations, *Phys. Rev. B* **43**, 1993 (1991).
- [34] J. P. Perdew, K. Burke, and M. Ernzerhof, Generalized Gradient Approximation Made Simple, *Phys. Rev. Lett.* **77**, 3865 (1996).

- [35] M. Büttiker, Y. Imry, R. Landauer, and S. Pinhas, Generalized many-channel conductance formula with application to small rings, *Phys. Rev. B* **31**, 6207 (1985).
- [36] See Supplemental Material at <http://link.aps.org/supplemental/10.1103/PhysRevApplied.22.014004> for further insights into the characteristics of the devices.
- [37] C. Heil, M. Schlipf, and F. Giustino, Quasiparticle  $GW$  band structures and Fermi surfaces of bulk and monolayer NbS<sub>2</sub>, *Phy. Rev. B* **98**, 075120 (2018).
- [38] S. Kim and Y.-W. Son, Quasiparticle energy bands and Fermi surfaces of monolayer NbSe<sub>2</sub>, *Phy. Rev. B* **96**, 155439 (2017).
- [39] K. D. Belashchenko, E. Y. Tsymbal, M. van Schilfgaarde, D. A. Stewart, I. I. Olynyk, and S. S. Jaswal, Effect of interface bonding on spin-dependent tunneling from the oxidized Co surface, *Phys. Rev. B* **69**, 174408 (2004).
- [40] T. Terzibaschian and R. Enderlein, The irreducible representations of the two-dimensional space groups of crystal surfaces. Theory and applications, *Physica Status Solidi (b)* **133**, 443 (1986).
- [41] M. S. Dresselhaus, G. Dresselhaus, and A. Jorio, *Group Theory: Application to the Physics of Condensed Matter* (Springer-Verlag, Berlin-Heidelberg, 2008).
- [42] N. F. Hinsche, M. Fechner, P. Bose, S. Ostanin, J. Henk, I. Mertig, and P. Zahn, Strong influence of complex band structure on tunneling electroresistance: A combined model and ab initio study, *Phys. Rev. B* **82**, 214110 (2010).
- [43] C. Herrmann, G. C. Solomon, J. E. Subotnik, V. Mujica, and M. A. Ratner, Ghost transmission: How large basis sets can make electron transport calculations worse, *J. Chem. Phys.* **132**, 024103 (2010).
- [44] L. Cheng, C. Zhang, and Y. Liu, Why Two-Dimensional Semiconductors Generally Have Low Electron Mobility, *Phys. Rev. Lett.* **125**, 177701 (2020).
- [45] A. Afzalian, Ab initio perspective of ultra-scaled CMOS from 2D-material fundamentals to dynamically doped transistors, *npj 2D Mater. Appl.* **5**, 1 (2021).
- [46] S. Smidstrup *et al.*, QuantumATK: An integrated platform of electronic and atomic-scale modelling tools, *J. Phys. Condens. Matter* **32**, 015901 (2019).